

DHGS: Decoupled Hybrid Gaussian Splatting for Driving Scene

Xi Shi*, **Lingli Chen***, **Peng Wei***, **Xi Wu[†]**, **Tian Jiang**, **Yonggang Luo**, **Lecheng Xie**

Changan Auto, AILab

{shixi, chenll4, weipeng4, wuxi, jiangtian, luoyg3, xielc}@changan.com.cn

Abstract

Existing Gaussian splatting methods struggle to achieve satisfactory novel view synthesis in driving scenes due to the lack of crafty design and geometric constraints of related elements. This paper introduces a novel method called Decoupled Hybrid Gaussian Splatting (DHGS), which aims at promoting the rendering quality of novel view synthesis for driving scenes. The novelty of this work lies in the decoupled and hybrid pixel-level blender for road and non-road layers, without conventional unified differentiable rendering logic for the entire scene, meanwhile maintaining consistent and continuous superimposition through the proposed depth-ordered rendering strategy. Beyond that, an implicit road representation comprised of Signed Distance Field (SDF) is trained to supervise the road surface with subtle geometric attributes. Accompanied by the use of auxiliary transmittance loss and consistency loss, novel images with imperceptible boundary and elevated fidelity are ultimately obtained. Substantial experiments on Waymo dataset prove that DHGS outperforms the state-of-the-art methods.

Introduction

The prevalence of 3DGS (Kerbl et al. 2023) has drawn numerous attentions in the community of 3D reconstruction and autonomous driving. Compared with NeRF-based approaches (Mildenhall et al. 2020; Barron et al. 2021), researchers who adopt Gaussian splatting are able to train and deploy a model in a more efficient and flexible way. Although Gaussian splatting technology has achieved immense performance in scene reconstruction, there are still imperfections in the novel view synthesis capabilities, which are particularly crucial for data synthesis tasks of autonomous driving scenes. Existing methods either model the whole driving scene in a consolidated manner (Kerbl et al. 2023; Huang et al. 2024a; Cheng et al. 2024; Lu et al. 2024), resulting in an even growing and pruning strategy for all types of scene elements, i.e. road, building, and distant views, or model the near scene and far sky (Wu et al. 2023; Miao et al. 2024) dividually. Above mentioned approaches emphasize the overall or specific far elements without the attention

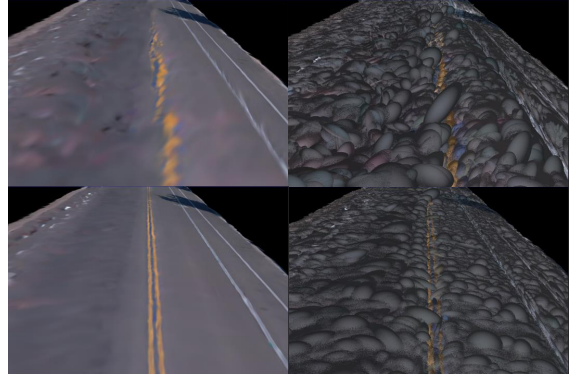


Figure 1: Comparative analysis of rendered images on novel view synthesis of road models is presented, the top row displaying results without SDF regularizer, and the bottom row showcasing results obtained using SDF regularizer. By visualizing corresponding ellipsoids, it can be observed that the inclusion of SDF regularization leads the road model to learn higher-quality geometric information.

to nearby synthesis quality. For real-world autonomous driving scenarios, the autonomous vehicle is usually on a smooth road equipped with several cameras with minimal overlapping fields of view, driving at a high speed. We reckon that the road should be maintained as the priority, since road-related geometrics play the basic role in downstream perceptual tasks and are brittle.

In this paper, we propose a method named Decoupled Hybrid Gaussian Splatting for Driving Scene (DHGS) for lifting the rendering quality of novel view synthesis, especially the nearby surroundings with fewer flaws and more subtle details. The insight of the method comes from the existing geometric prior that could be utilized to supervise the nearby road elements along with other non-road environments in a fancy pattern. Specifically, we decouple the whole driving scene into a nearby road model and environment model represented by two separate Gaussian models, considering optimizing the two models based on their geometric characters accordingly. Before that, we project and segment the point clouds using semantic 2D masks to obtain the initial road point cloud and environmental point cloud. The road point cloud is used for pre-training the implicit Signed Distance

*These authors contributed equally.

[†]Corresponding author.

Field (SDF). The training process is conducted via the introduced depth-ordered rendering strategy by the blender of rendered images of both models, assisted with transmittance loss that regularizes the accumulated transmittance of each component Gaussian properties, as well as consistency loss which bonds the two areas compactly. Besides, we optimize the road elements using SDF loss that is expressly designed for surface regularization, reaching consistent and orderly road Gaussians. To summarize, the contributions of the proposed DHGS are listed as follows:

- We first propose to decouple the driving scene into near road model and other non-road model, enabling the optimization separately of two models and rendering jointly with the designed depth-ordered rendering strategy,
- We propose an implicit road represent for better guidance of road Gaussian, alone with transmittance loss and consistency loss that guarantee continuity and consistency,
- Abundant quantitative and qualitative experiments on the popular Waymo dataset demonstrate that DHGS achieves state-of-the-art rendering qualities on training views and brand-new free-view synthesis.

Related Works

Neural Radiance Field Representations

NeRF (Mildenhall et al. 2020) has attracted remarkable attention in the field of view synthesis, which adopts Multi-Layer Perceptron (MLP) to implicitly model the 3D scene. NeRF takes the spatial coordinates and the viewing directions of the sample point as input to MLP and predicts the color and opacity of each point in the camera ray, then accumulates into pixel color by neural volume rendering. For each pixel, necessitating the sampling of hundreds of points and subsequent prediction of their attributes via an MLP, leading to extremely slow training and rendering phases. Besides, the finite number of sampling points limits the expression ability in complex and large-scale driving scenes. Mip-NeRF (Barron et al. 2021) proposes a more efficient sampling strategy, where the sampling region is improved from a single ray to a frustum of a viewing cone. Mip-NeRF 360 (Barron et al. 2022) and NeRF++ (Zhang et al. 2020) divide the scene into near and far regions, and apply warping operations to the far regions to handle the unbounded 3D scene. Instant-NGP (Müller et al. 2022) uses a hash grid to store features and reduces the MLP size to release the computational burden. Plenoxels Fridovich-Keil et al. (2022) makes use of sparse grids to reduce storage space and utilizes Spherical Harmonics (SH) to represent the appearance. These methods are based on the data captured by 360-degree object-centric trajectory, while free and long driving scenes draw less attention. F2-NeRF (Wang et al. 2023) proposes a novel space-warping method that supports arbitrary input camera trajectories, enabling the reconstruction of driving scenes. StreetSurf (Guo et al. 2023) extends prior object-centric neural surface reconstruction techniques to address the unique challenges posed by the unbounded street views, showing potential for various downstream tasks. The aforementioned approaches remain a trade-off between render-

ing quality and efficiency, thereby limiting the application in large-scale autonomous driving scenarios.

Gaussian Splatting Representations

3DGS (Kerbl et al. 2023) is a seminal work that pioneers the use of 3D Gaussian ellipsoids to explicitly represent a scene and leverages CUDA for parallel rendering, achieving rendering quality and speed that far exceed NeRFs. It integrates pixel colors using α -blending and performs adaptive density control, thus the input only requires sparse point clouds. A number of works have been proposed for large-scale scene 3D reconstruction based on 3DGS. VastGaussian (Lin et al. 2024) tackles large scenes with novel designs for scene partitioning, optimizing, and merging. HUGS (Zhou et al. 2024a) offers the ability to render novel views in real-time, yielding 2D and 3D semantic information with high accuracy.

The vanilla 3DGS only fits the consistency of pixel colors, neglecting to model the geometric structure. Consequently, obvious discontinuities such as artifacts and holes appear under unseen views. This discontinuity phenomenon would be more prominent on training datasets with sparse views. DRGS (Chung, Oh, and Lee 2024) introduces a dense depth map as a geometry guide to mitigate overfitting. AtomGS (Liu et al. 2024) introduces an atomized proliferation strategy aimed at enhancing rendering quality by refining 3D geometric precision in areas with fine details. NeuSG (Chen, Li, and Lee 2023) flattens the Gaussian ellipsoid by designing a regularization loss for the scale parameter, and performs consistent joint optimization in combination with the signed distance field. SuGaR (Guédon and Lepetit 2024) first proposes adding a regularization term to encourage the alignment of the Gaussian with the surface, thereby achieving accurate and fast mesh extraction. Scaffold GS (Lu et al. 2024) precisely controls the density of the Gaussian ellipsoid by establishing voxel anchors and corresponding offset vectors, and learning the various parameters of the Gaussian through a simple multi-layer network. Gaussian Pro (Cheng et al. 2024) considers the planar prior in the scene, explicitly constraining the growth of Gaussians, achieving amendatory rendering and more compact representation. 2DGS (Huang et al. 2024a) presents a highly efficient differentiable 2D Gaussian renderer, enabling perspective-accurate splatting by leveraging 2D surface modeling, demonstrating superiority in geometric reconstruction.

Reconstructing a reliable scene geometry plays a pivotal role in driving data synthesis techniques for 3DGS-like approaches. Driving Gaussians (Zhou et al. 2024b), Street Gaussians (Yan et al. 2024) and S³ Gaussians (Huang et al. 2024b) all initialize the point cloud collected by LiDAR instead of the point cloud generated by SfM. With the use of dense and precise point clouds from LiDAR, additional supervision, such as the positional constraint, is introduced to the learning process.

Existing works pay less attention to the ability of novel view synthesis, leading to low-grade image quality when imposed remarkable camera transformation. We propose to address this shortcoming by decoupling the entire scene into two distinct models, employing optimization separately.

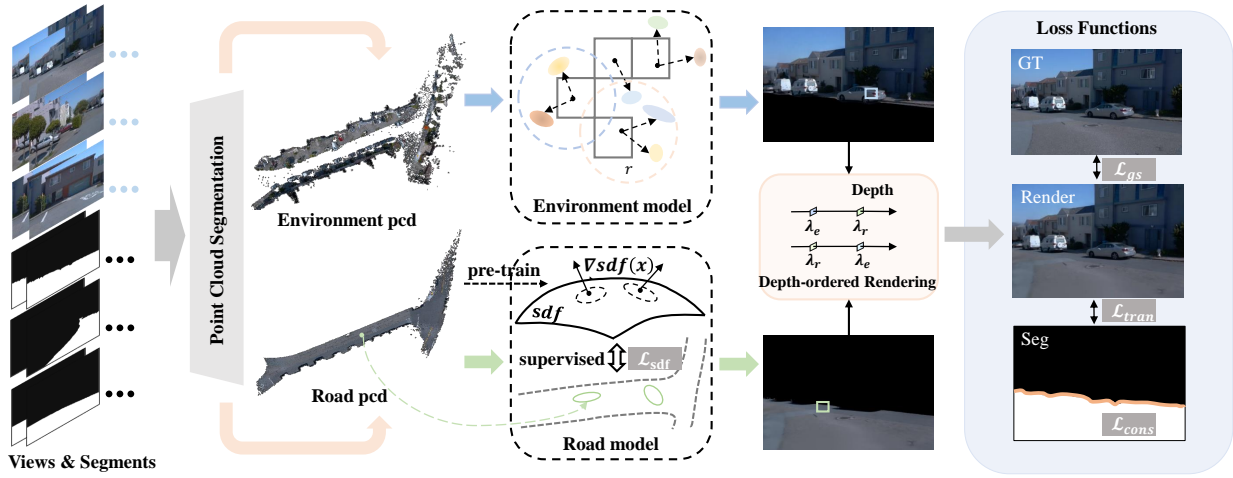


Figure 2: The pipeline of the proposed method for driving scene reconstruction. For consecutive multi-camera images and corresponding road and non-road masks, we firstly generate decoupled road pcd (point cloud) and environment pcd, a road SDF is then pre-trained as the following supervision for road gaussian model. Environment pcd enables the initialization for environment Gaussian model which composes rendered images with images by paratactic road model via proposed Depth-ordered rendering.

Preliminary

3DGS utilizes a set of 3D Gaussians to explicitly represent a scene, achieving high-fidelity rendering quality and fast speed via tile-based rasterization. Each Gaussian G is defined as:

$$G(\mathbf{x}) = e^{-\frac{1}{2}(\mathbf{x}-\boldsymbol{\mu})^\top \boldsymbol{\Sigma}^{-1}(\mathbf{x}-\boldsymbol{\mu})}, \quad (1)$$

where $\boldsymbol{\mu}$ is the mean position of Gaussian and the \mathbf{x} is a disretional coordinate within the Gaussian space. $\boldsymbol{\Sigma} = R S S^T R^T$, where R is the rotation matrix and S is the scaling matrix. Apart from the spherical harmonic coefficients that represent the anisotropic color of each Gaussian, each pixel color is aggregated by α -blending:

$$\mathbf{c}(\mathbf{x}) = \sum_{i=1}^N \mathbf{c}_i \alpha_i \prod_{j=1}^{i-1} (1 - \alpha_j), \quad (2)$$

where α_i is the opacity of the 2D Gaussian projected from 3D Gaussian to the 2D image plane and \mathbf{c}_i is the color of the Gaussian in the view direction.

2DGS ensures multi-view consistency well by adopting the expression of surfels and using the projection method specifically for surfels. It achieves 2D Gaussian rendering through ray-splat intersection. The process of ray-splat intersection can be written as:

$$u(\mathbf{x}) = \frac{\mathbf{h}_u^2 \mathbf{h}_v^4 - \mathbf{h}_u^4 \mathbf{h}_v^2}{\mathbf{h}_u^1 \mathbf{h}_v^2 - \mathbf{h}_u^2 \mathbf{h}_v^1}, \quad v(\mathbf{x}) = \frac{\mathbf{h}_u^4 \mathbf{h}_v^1 - \mathbf{h}_u^1 \mathbf{h}_v^4}{\mathbf{h}_u^1 \mathbf{h}_v^2 - \mathbf{h}_u^2 \mathbf{h}_v^1}, \quad (3)$$

where \mathbf{h}_u , \mathbf{h}_v are two planes represented in homogeneous coordinates. By defining the function $G(\mathbf{u}) = \exp\left(-\frac{u^2+v^2}{2}\right)$, and employing the object-space low-pass filter $\hat{G}(\mathbf{x}) = \max\{G(\mathbf{u}(\mathbf{x})), G(\frac{\mathbf{x}-\mathbf{c}}{\sigma})\}$, the rasterization

for 2DGS can be shown as:

$$\mathbf{c}(\mathbf{x}) = \sum_{i=1}^N \mathbf{c}_i \alpha_i \hat{G}_i(\mathbf{u}(\mathbf{x})) \prod_{j=1}^{i-1} (1 - \alpha_j \hat{G}_j(\mathbf{u}(\mathbf{x}))). \quad (4)$$

Method

Overview

The proposed method utilizes initial points clouds and semantic masks as paratactic input of multi-camera views. PCD initialization first generates road and non-road point clouds that will be further modeled as road and environment Gaussian model. Based on the known road point cloud, we propose to design a mathematical implicit road representation by SDF which serves as a prior for the surface training. The SDF-based surface constraint consists of pre-training and off-line supervision phases, by taking advantage of the distance and normal characters geometrically. We choose to model road and non-road elements with two kinds of Gaussians for better rendering quality in perspective shifts. To achieve that, depth-ordered hybrid rendering is delicately designed, by which the road surface and non-road areas can be coupled and superimposed consistently and continuously, yielding superior performance compared with SOTA methods that employ individual Gaussian model. The rendered image by fusing two models will be supervised by ground truth via Gaussian loss, and optimized in collaboration with the regularization terms. We will go through the process in turn in the following sections.

PCD Initialization

Different from previous approaches, we opt to utilize LiDAR scan which exhibits better multi-view consistency and prior geometric structure compared to the point cloud from

SfM. The initial point cloud is classified into road and non-road parts for the subsequent training. As shown in Figure 2, based on the calibrated intrinsic and extrinsic parameters, multi-camera images and their masks generated by Mask2Former (Cheng et al. 2022) are utilized to form colored and semantically labeled single-frame point clouds. Then we stitch these separate point clouds to build road and environment point clouds.

Pre-trained Surface Base On SDF

To optimize the geometric structure of roads and maintain the continuity when facing obvious changes in perspective, we design a road constraint based on surface guidance. Taking advantage of the separated road point cloud, we pre-train a signed distance field as an implicit representation of the real road surface. This manner differs from the joint ray sampling optimization in NeRF and the guidance of geometric structure and image consistency in GSDF (Yu et al. 2024). As road point clouds collected by LiDAR have been calibrated precisely in advance, the excellent geometric structure is suitable to be prior for road learning. A straightforward strategy is directly applying distance constraints to Gaussians that belong to road. Whereas, considering the spatial geometric characteristics of ellipsoids, imposing constraints only on the centers of Gaussian ellipsoids cannot fully restore their correct geometric shapes and may ultimately limit the Gaussian distribution to some extent. We therefore adopt a pre-trained model to optimize the Gaussian distribution by adjusting Gaussian parameters nearing the road surface. To this end, we design several regularization terms specific to road-related Gaussians, including distance constraints and normal direction constraints, forcing Gaussians to be close to the road surface and directional aligned with the road normal synchronously.

We utilize a predefined network $f_\theta(x)$ for predicting the corresponding SDF value given the positional coordinate of the point cloud. Data normalization is imposed on all the training and testing coordinates for stable and better performance. For balancing the number of points on the isosurface and off the isosurface, we make training data as follows. Suppose that \mathcal{P}_r represents the road point cloud, each point $x_p \in \mathcal{P}_r$ meanwhile on isosurface will be assigned a hypothetical SDF value of 0. For other points off the isosurface, we set a nearby range for each point in \mathcal{P}_r and conduct random sampling within that region, thus obtaining sample points $\mathcal{P}_s \supset \mathcal{P}_r$, for $\forall x_s \in \mathcal{P}_s$ we build a map from point x_s to the signed euclidean distance d_s as:

$$d_s = \text{sgn}(x_s^{(3)} - x_r^{(3)}) \cdot \|x_s - x_r^s\|_2, \quad (5)$$

where x_r^s is the nearest point of x_s in \mathcal{P}_r . Considering that bumps exist in the uneven road surfaces, we generate the normal direction for each point in \mathcal{P}_r to assist in the training the SDF. To be specific, for $\forall x_r \in \mathcal{P}_r$, set X_r as k -nearest neighbors of x_r , by performing SVD:

$$U \Lambda V^T = \text{svd}(\tilde{X}), \quad (6)$$

where $\tilde{X} \triangleq X_r - \bar{X}_r$. The right singular vector v_i corresponding to the minimum singular value λ_i is finally regarded as the normal of x_r , noted as n_r .

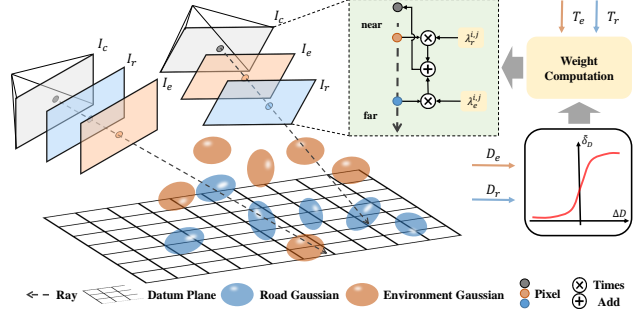


Figure 3: The schematic of the proposed depth-ordered hybrid rendering strategy for the environment and road model. Corresponding primitives of each model generate pixels with colors independently through Gaussian splatting. These colors are then composited based on their rendered depths and transmittances, producing the final rendered image.

We supervise the predicted SDF value from the network with our pre-computed ground truth by incorporating a newly proposed normal loss based on the predicted normal direction. The optimization goal of road SDF is written as:

$$\begin{aligned} \min_{\theta} \{L(\theta) := & \frac{1}{|\mathcal{P}_s|} \sum_{x_s \in \mathcal{P}_s} \|f_\theta(\tilde{x}_s) - d_s\|_2^2 \\ & + \frac{1}{|\mathcal{P}_r|} \sum_{x_r \in \mathcal{P}_r} \{\lambda_n \sin^2 \langle \nabla f_\theta(\tilde{x}_r), n_r \rangle \\ & + \lambda_{\text{eik}} (\|\nabla f_\theta(\tilde{x}_r)\|_2 - 1)^2\}\}, \end{aligned} \quad (7)$$

in which the first and last terms refer to SDF value regularization and eikonal regularizer respectively, the middle term represents normal loss, $|\cdot|$ refers to the number of points in the point cloud. The optimal parameters $\theta^* = \arg \min_{\theta} L(\theta)$ will be frozen and used to guide the learning of road Gaussians in the following processes.

Depth-Ordered Hybrid Rendering

Based on the predefined initial semantic non-road point cloud \mathcal{P}_e and road point cloud \mathcal{P}_r , we build the environment model and road model simultaneously. In this paper, Scaffold GS and 2DGs are chosen as the fundamental Gaussian splatting substrates. By executing forward rendering separately, output images I_e and I_r , as well as depth maps and accumulated transmittance maps will be generated in parallel. In our experiments, simply fusing I_e and I_r linearly causes inferior image quality. The reason is that naive fusion degrades the learning of Gaussian properties without the solicitude for real depth relationship of Gaussians from the environment and road model. The depth D is rendered based on d_i that indicates each splat from the camera, following the rasterization pipeline in (Dai et al. 2024; Chung, Oh, and Lee 2024),

$$D = \sum_{i=1}^N d_i \alpha_i \prod_{j=1}^{i-1} (1 - \alpha_j), \quad T = \prod_{i=1}^N (1 - \alpha_i).$$

Accordingly, we adopt a pixel-level hybrid rendering method based on depth sorting, as depicted in Figure 3. Assuming that the tuple $[I_e, D_e, T_e]$ severally represents image,

Metrics	Scene Reconstruction			Novel View Synthesis			Free-view Novel View Synthesis			
	PSNR↑	SSIM↑	LPIPS↓	PSNR↑	SSIM↑	LPIPS↓	FID↓			
							Set1	Set2	Set3	Set4
3DGS	26.91	0.8295	0.3101	25.92	0.8089	0.3218	53.12	61.93	82.52	61.53
2DGS	24.75	0.7919	0.3746	24.26	0.7819	0.3798	101.9	105.5	123.4	105.6
Gaussian Pro	25.90	0.8019	0.3250	25.09	0.7827	0.3358	60.52	68.75	90.12	69.05
Scaffold GS	<u>28.04</u>	<u>0.8428</u>	<u>0.3039</u>	26.87	0.8224	<u>0.3142</u>	<u>51.93</u>	<u>58.25</u>	<u>78.64</u>	<u>57.85</u>
Ours	28.09	0.8460	0.2960	<u>26.77</u>	<u>0.8216</u>	0.3100	48.05	56.93	75.72	55.52

Table 1: The quantitative comparison between our method with four SOTA works on PSNR, SSIM, LPIPS and FID metrics computed over all clips on Waymo dataset. We adopt the same training data for each method and follow the corresponding experimental settings strictly. The best and second best are marked in **bold** and underline for each metric of specific setting, respectively.

depth, and accumulated transmittance rendered by the environment model, $[I_r, D_r, Tr]$ indicates image, depth, and accumulated transmittance rendered by the road model in the same manner. The composite rendering strategy is presented as:

$$I_c = \lambda_r I_r + \lambda_e I_e, \quad (8)$$

where λ_r and λ_e are the weights for fusing I_r and I_e rendered from environment model and road model respectively, which are organized as:

$$\begin{aligned} \lambda_r &= T_e \delta_D + (1 - \delta_D), \\ \lambda_e &= T_r (1 - \delta_D) + \delta_D, \end{aligned} \quad (9)$$

where δ_D is the item for composing weights of fusion, which is defined as:

$$\delta_D = \begin{cases} 1 & D_r > D_e \\ 0 & D_r \leq D_e \end{cases} \quad (10)$$

One limitation of blending the rendered images discontinuously is that the weights also vary discretely, which will result in the distinct appearance of boundary lines on the edge of road and non-road regions. We thus introduce a consecutive strategy to model the dynamic weights based on the rendered depth. Concretely, the sigmoid function $S(x)$ is utilized to realize the ordered rendering as:

$$S(x) = \frac{1}{1 + \exp(-s_\sigma x)}, \quad (11)$$

where s_σ is a given hyperparameter. We set $\Delta D = D_r - D_e$ indicating depth difference as the input of $S(x)$ to obtain $\tilde{\delta}_D = S(\Delta D)$, the smoother weights can be shown as:

$$\begin{aligned} \lambda_r &= T_e \tilde{\delta}_D + (1 - \tilde{\delta}_D), \\ \lambda_e &= T_r (1 - \tilde{\delta}_D) + \tilde{\delta}_D. \end{aligned} \quad (12)$$

With the proposed smooth rendering mechanism, the overall rendering quality can be significantly improved and the synthesis of new perspectives will appear more natural and fluid.

Loss Functions

The overall training objective is given as follows:

$$\mathcal{L} = \mathcal{L}_{\text{gs}} + \lambda_{\text{tran}} \mathcal{L}_{\text{tran}} + \lambda_{\text{sdf}} \mathcal{L}_{\text{sdf}} + \lambda_{\text{cons}} \mathcal{L}_{\text{cons}} + \lambda_{\text{tv}} \mathcal{L}_{\text{tv}}, \quad (13)$$

among which \mathcal{L}_{gs} is responsible for measuring the reconstruction discrepancy used in 3DGS:

$$\mathcal{L}_{\text{gs}} = \lambda \mathcal{L}_1(I_c, I_{gt}) + (1 - \lambda) \mathcal{L}_{\text{D-SSIM}}(I_c, I_{gt}), \quad (14)$$

where I_{gt} is the ground truth. The \mathcal{L}_{sdf} consists of two parts, distance loss and normal loss of the road surface, written as:

$$\mathcal{L}_{\text{sdf}} = \frac{1}{N} \sum_{i=1}^N \{ \lambda_d \|f_{\theta^*}(\tilde{x}_i)\|_1 + \lambda_n \sin^2 \langle \nabla f_{\theta^*}(\tilde{x}_i), t_n \rangle \}, \quad (15)$$

where $t_n = t_u \times t_v$ refers to 2D primitive normal of Gaussian. $\mathcal{L}_{\text{tran}}$ supervises the accumulated transmittance of road and non-road regions, ensuring their consistency with the corresponding regions in the 2D semantic segmentation, which is represented as:

$$\mathcal{L}_{\text{tran}} = \frac{1}{|M|} (\|T_e - M\|_F^2 + \|T_r - (1 - M)\|_F^2), \quad (16)$$

where M refers to the semantic mask of the image, $|\cdot|$ denotes the total number of pixels for given matrix. The \mathcal{L}_{c} enforces consistency between the depth rendered by environment gaussians and road gaussians:

$$\mathcal{L}_{\text{cons}} = \max_j \min_i |D_e^{i,j} - D_r^{i,j}|, \quad (17)$$

where i and j satisfying $\tilde{M}^{i,j} \neq 0$, \tilde{M} refers to the banded boundary generated by binary mask M , and the orange band at the bottom right corner of Figure 2 intuitively shows the distribution of elements in \tilde{M} . We follow Plenoxels (Fridovich-Keil et al. 2022) and use a total variation loss \mathcal{L}_{tv} . Through the joint efforts of abovementioned loss functions, DHGS is able to obtain high-quality render views with continuous geometric structure.

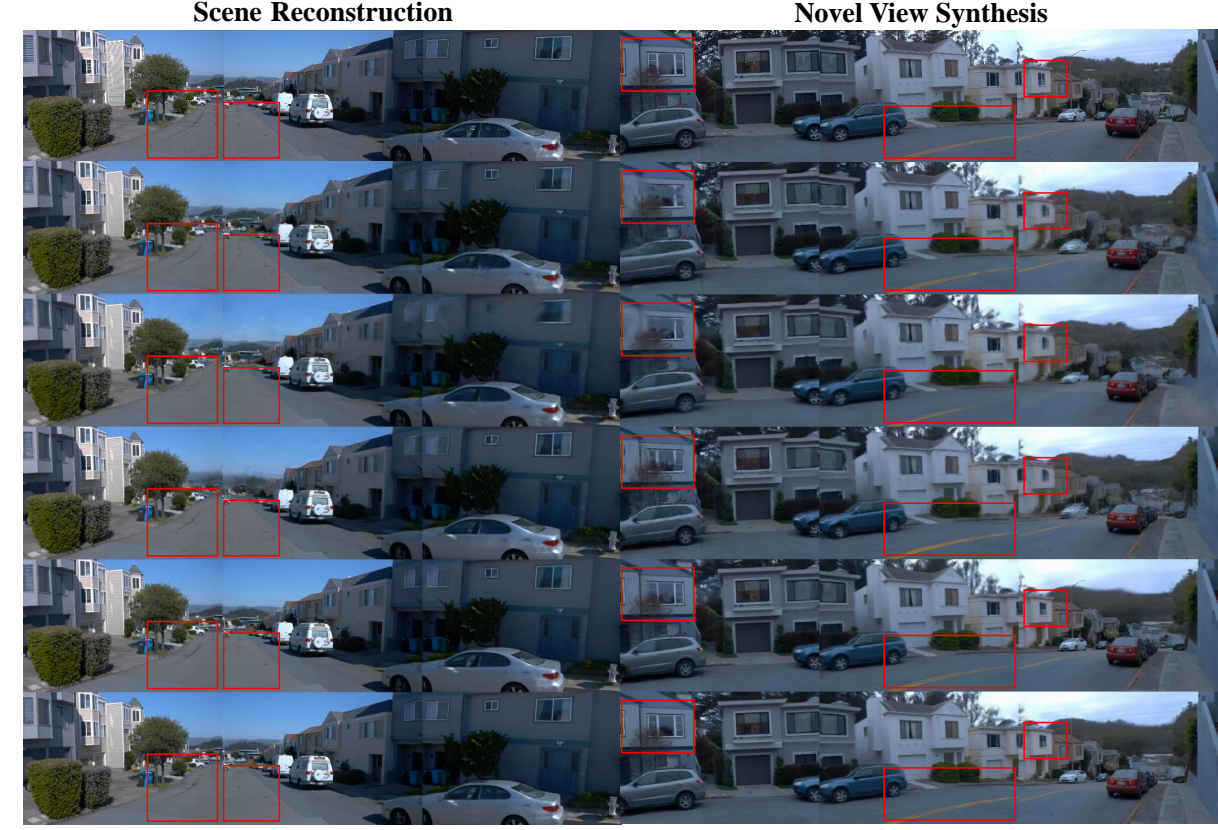


Figure 4: Comparison of different methods on Waymo dataset, the left column and right column showcase the quality of scene reconstruction and novel view synthesis respectively. Our method achieves high-quality reconstruction for both the environment region and the road region, outperforming other comparative methods in both aspects.

Experiments and Analysis

Experimental Settings

Datasets and Metrics. We experiment on the publicly available urban scene datasets Waymo (Sun et al. 2020), 32 static scenes are adopted as the same as EmerNeRF (Yang et al. 2023). We employ multiple metrics to evaluate the performance of the proposed method and baselines. PSNR, SSIM, and LPIPS metrics are utilized to validate the quality of rendered images with ground truth. For novel views without ground truth, we introduce FID (Heusel et al. 2017) to evaluate the image quality. The averaged metrics across all clips are calculated as comparative values.

Baselines. We compare our method with state-of-the-art and publicly available works. 3DGS (Kerbl et al. 2023), 2DGS (Huang et al. 2024a), Gaussian Pro (Cheng et al. 2024), and Scaffold GS (Lu et al. 2024) are chosen as the comparison methods having regarded to their outstanding performances.

Implementation details. The initial point cloud is randomly downsampled to 600,000 points. All methods are trained for 60,000 iterations. For the pre-trained SDF network, we employ an 8-layer MLP and train it for 20,000 iterations. The normals of surface points are computed using SVD with 50 neighbors, and the weights for the normal loss and the eikonal loss of the SDF network are set to 0.1 and 0.01. The

weights λ_{tran} , λ_{sdf} , λ_{cons} , λ_{tv} , λ_d and λ_n of the overall training loss are set to 0.1, 1.0, 0.04, 0.1, 0.1 and 0.1. We set the densification intervals for the Gaussian ellipsoids in the environment model and road model to 200 and 300 respectively. The learning rate for anchor position in the environment model is set as 0.00016, the remaining learning rates are kept consistent with the original settings. For each clip, we utilize all the front, left-front, and right-front views of the entire sequence for training, with a 4:1 split ratio between the training and testing sets. The training set is referred to as the reconstruction views, while the testing set is called the novel views. We further apply unrestricted transformations on camera poses to validate the potential of model on data-driven simulation, which is referred to as free-view novel view synthesis.

Comparisons

We compare against baseline methods on scene reconstruction, novel view synthesis, and free-view novel view synthesis that represents notable viewpoints transfer. All methods use the same set of reconstruction views to train and use the rest as novel views to test for each clip. The qualitative and quantitative results will be analyzed in the following sections, where the ablation study is also conducted.

Free-view Novel View Synthesis



Figure 5: Visual comparisons on the free-view novel view synthesis. The left and right columns respectively showcase the results of *Set3* and *Set4* under the free viewpoint setting, where our method significantly outperforms other comparative methods in both road and environment details.

Scene Reconstruction on Waymo Dataset. For reconstruction views, we calculate the mean PSNR, SSIM, and LPIPS of the rendered images for 32 clips as shown in Table 1. Our method outperforms all the mainstream methods: including 3DGS, 2DGS, Gaussian Pro and Scaffold GS. The left part of Figure 4 shows the rendered images of the reconstruction views from our method and the comparison methods. It can be noticed that our method achieves better reconstruction quality with finer details than competitive methods, from which the road area rendered by our method contains richer texture information.

Novel View Synthesis on Waymo dataset. We evaluate the aforementioned methods on the novel views. Table 1 illustrates the validation results, our method surpasses most rival methods, such as 3DGS, 2DGS and Gaussian Pro, and achieves comparable results to Scaffold GS. Here Scaffold GS gets the best performance on PSNR and SSIM. As depicted in the right part of Figure 4, blurriness arises in some non-road areas (framed in red boxes) for 3DGS, 2DGS, and Gaussian Pro. Meanwhile, our method restores more road details (lane lines within the red boxes) due to the imposition of geometric constraints on the road, whereas other methods such as 2DGS, Gaussian Pro, and Scaffold GS fail to retain these details.

Free-view Novel View Synthesis on Waymo dataset. Although the novel views are not utilized for training, the changes in their camera poses are relatively small compared to the trained views, along with no variation in the rela-

tive position of the cameras to the vehicle, which can be simply concluded as the interpolation of trained views. To further demonstrate the free-view novel view synthesis performance of our method, evaluating the trained model on greater pose variations of cameras, we vary the poses of the cameras relative to the vehicle, simulating various observation perspectives for different vehicle types with diverse camera positions. In this paper, we perform four transformations on the camera poses, the specific configurations are detailed in the supplemental material. Since there is no ground truth for the free-view novel views, we adopt FID metric that is able to effectively measure the feature gap between the distributions of the origin input views and the free-view novel views. The comparisons of FID for free-view novel views are also presented in Table 1, where our method achieves the highest performance compared to other methods in all four configurations with considerable preponderance. The qualitative render results are shown in Figure 5, where the free-view rendered images produced by other methods suffer from extensive artifacts and lane line breakage. Our method is still able to render complete road details such as lane lines and environmental details even after significant changes in the camera pose. The above results further confirm that the regularization constraints we proposed can ensure the model learns a more optimal geometric road structure, thereby showcasing the robust capabilities of our approach in untrammelled novel view synthesis. More visual comparisons can be found in supplemental materials.



Figure 6: Qualitative comparison for free-view novel views of ablation results. The highlighted patches demonstrate that these regularization terms are all beneficial to the reconstruction of road geometry.

Ablation Study.

To validate the effectiveness of the proposed regularization components, we conduct an ablation study. We train our proposed method by separately removing the SDF loss, transmittance loss and consistency loss, denoted as "w/o SDF", "w/o trans", and "w/o cons" respectively. The quantitative indexes of scene reconstruction, novel view synthesis and free-view novel view synthesis are presented in Table 2. For scene reconstruction and novel view synthesis, removing the SDF loss leads to a decline in various metrics, while removing the transmittance loss and consistency loss does not result in significant drop. However, for free-view novel view synthesis, removing any of the losses leads to an increase in the FID score, indicating a larger discrepancy between the novel views and the original images. To more intuitively illustrate the specific contributions of these components, we give the visualization results of free-view novel views synthesis in Figure 6. When we remove the SDF regularization term, the traffic sign characters on the road undergo noticeable distortions. When the consistency regularization term is removed, a clear dark seam emerges between the road and the environment. If the transmittance regularization term is removed, large areas of artifacts appear on the road. These regularization terms each play their own role. Specifically, the SDF loss ensures the correctness of road geometry, the consistency loss guarantees a seamless connection between the environment model and the road model. The transmittance Loss ensures that the rendering areas of the road model and the environment model accurately align with the 2D semantic segmentation map, thereby preventing the occurrence of artifacts when rendering novel views.

Conclusions

In this paper, we propose a novel reconstruction method called DHGS, which aims to enhance the rendering quality of novel view synthesis for driving scenes. The method uses two models to model the road and environment respectively, and introduces a pixel-level blending renderer that

Metrics	w/o SDF	w/o tran	w/o cons	Ours
<i>Scene Reconstruction</i>				
PSNR↑	27.76	28.18	28.01	28.09
SSIM↑	0.8381	0.8473	0.8453	0.8460
LPIPS↓	0.3147	0.2934	0.3007	0.2961
<i>Novel View Synthesis</i>				
PSNR↑	26.29	26.63	26.68	26.77
SSIM↑	0.8151	0.8213	0.8205	0.8217
LPIPS↓	0.3195	0.3113	0.3154	0.3100
<i>Free-view Novel View Synthesis</i>				
FID↓	61.16	61.02	62.49	59.06

Table 2: Quantitative results of ablation experiments on Waymo dataset, with each metric averaged across all clips.

overlays the rendered layers of these two models through the proposed depth-ordered rendering strategy. Additionally, consistency loss and transmittance loss are proposed to constrain the fundamental models, enabling the generation of continuous and consistent rendered images. Furthermore, we propose a road surface regularization term based on SDF to ensure better geometric consistency of the road surface, guaranteeing stable image quality as perspective changes. We conduct comprehensive experiments on the Waymo dataset, revealing the state-of-the-art performance in both reconstruction and novel view synthesis of our method.

Acknowledgments

This work would thank Bo Zheng and Fan Jin for providing necessary help in the preparation of training data.

References

Barron, J. T.; Mildenhall, B.; Tancik, M.; Hedman, P.; Martin-Brualla, R.; and Srinivasan, P. P. 2021. Mip-nerf: A multiscale representation for anti-aliasing neural radiance fields. In *Proceedings of the IEEE/CVF International Conference on Computer Vision (ICCV)*, 5855–5864.

Barron, J. T.; Mildenhall, B.; Verbin, D.; Srinivasan, P. P.; and Hedman, P. 2022. Mip-nerf 360: Unbounded anti-aliased neural radiance fields. In *Proceedings of the IEEE/CVF Conference on Computer Vision and Pattern Recognition (CVPR)*, 5470–5479.

Chen, H.; Li, C.; and Lee, G. H. 2023. Neusg: Neural implicit surface reconstruction with 3d gaussian splatting guidance. *arXiv preprint arXiv:2312.00846*.

Cheng, B.; Misra, I.; Schwing, A. G.; Kirillov, A.; and Girdhar, R. 2022. Masked-attention mask transformer for universal image segmentation. In *Proceedings of the IEEE/CVF Conference on Computer Vision and Pattern recognition (CVPR)*, 1290–1299.

Cheng, K.; Long, X.; Yang, K.; Yao, Y.; Yin, W.; Ma, Y.; Wang, W.; and Chen, X. 2024. Gaussianpro: 3d gaussian splatting with progressive propagation. *arXiv preprint arXiv:2402.14650*.

Chung, J.; Oh, J.; and Lee, K. M. 2024. Depth-regularized optimization for 3d gaussian splatting in few-shot images. In *Proceedings of the IEEE/CVF Conference on Computer Vision and Pattern Recognition (CVPR)*, 811–820.

Dai, P.; Xu, J.; Xie, W.; Liu, X.; Wang, H.; and Xu, W. 2024. High-quality surface reconstruction using gaussian surfels. *arXiv preprint arXiv:2404.17774*.

Fridovich-Keil, S.; Yu, A.; Tancik, M.; Chen, Q.; Recht, B.; and Kanazawa, A. 2022. Plenoxels: Radiance fields without neural networks. In *Proceedings of the IEEE/CVF Conference on Computer Vision and Pattern Recognition (CVPR)*, 5501–5510.

Guédon, A., and Lepetit, V. 2024. Sugar: Surface-aligned gaussian splatting for efficient 3d mesh reconstruction and high-quality mesh rendering. In *Proceedings of the IEEE/CVF Conference on Computer Vision and Pattern Recognition (CVPR)*, 5354–5363.

Guo, J.; Deng, N.; Li, X.; Bai, Y.; Shi, B.; Wang, C.; Ding, C.; Wang, D.; and Li, Y. 2023. Streetsurf: Extending multi-view implicit surface reconstruction to street views. *arXiv preprint arXiv:2306.04988*.

Heusel, M.; Ramsauer, H.; Unterthiner, T.; Nessler, B.; and Hochreiter, S. 2017. Gans trained by a two time-scale update rule converge to a local nash equilibrium. *Advances in Neural Information Processing Systems (NIPS)* 30.

Huang, B.; Yu, Z.; Chen, A.; Geiger, A.; and Gao, S. 2024a. 2d gaussian splatting for geometrically accurate radiance fields. *arXiv preprint arXiv:2403.17888*.

Huang, N.; Wei, X.; Zheng, W.; An, P.; Lu, M.; Zhan, W.; Tomizuka, M.; Keutzer, K.; and Zhang, S. 2024b. S³ gaussian: Self-supervised street gaussians for autonomous driving. *arXiv preprint arXiv:2405.20323*.

Kerbl, B.; Kopanas, G.; Leimkühler, T.; and Drettakis, G. 2023. 3d gaussian splatting for real-time radiance field rendering. *ACM Transactions on Graphics (TOG)* 42(4):1–14.

Lin, J.; Li, Z.; Tang, X.; Liu, J.; Liu, S.; Liu, J.; Lu, Y.; Wu, X.; Xu, S.; Yan, Y.; et al. 2024. Vastgaussian: Vast 3d gaussians for large scene reconstruction. *arXiv preprint arXiv:2402.17427*.

Liu, R.; Xu, R.; Hu, Y.; Chen, M.; and Feng, A. 2024. Atomgs: Atomizing gaussian splatting for high-fidelity radiance field. *arXiv preprint arXiv:2405.12369*.

Lu, T.; Yu, M.; Xu, L.; Xiangli, Y.; Wang, L.; Lin, D.; and Dai, B. 2024. Scaffold-gs: Structured 3d gaussians for view-adaptive rendering. In *Proceedings of the IEEE/CVF Conference on Computer Vision and Pattern Recognition (CVPR)*, 20654–20664.

Miao, S.; Huang, J.; Bai, D.; Qiu, W.; Liu, B.; Geiger, A.; and Liao, Y. 2024. Edus: Efficient depth-guided urban view synthesis. In *European Conference on Computer Vision (ECCV)*.

Mildenhall, B.; Srinivasan, P.; Tancik, M.; Barron, J.; Ramamoorthi, R.; and Ng, R. 2020. Nerf: Representing scenes as neural radiance fields for view synthesis. In *European conference on computer vision*.

Müller, T.; Evans, A.; Schied, C.; and Keller, A. 2022. Instant neural graphics primitives with a multiresolution hash encoding. *ACM Transactions on Graphics (TOG)* 41(4):1–15.

Rudin, L. I., and Osher, S. 1994. Total variation based image restoration with free local constraints. In *Proceedings of 1st international conference on image processing*, volume 1, 31–35. IEEE.

Sun, P.; Kretzschmar, H.; Dotiwalla, X.; Chouard, A.; Patnaik, V.; Tsui, P.; Guo, J.; Zhou, Y.; Chai, Y.; Caine, B.; et al. 2020. Scalability in perception for autonomous driving: Waymo open dataset. In *Proceedings of the IEEE/CVF Conference on Computer Vision and Pattern Recognition (CVPR)*, 2446–2454.

Wang, P.; Liu, Y.; Chen, Z.; Liu, L.; Liu, Z.; Komura, T.; Theobalt, C.; and Wang, W. 2023. F2-nerf: Fast neural radiance field training with free camera trajectories. In *Proceedings of the IEEE/CVF Conference on Computer Vision and Pattern Recognition (CVPR)*, 4150–4159.

Wu, Z.; Liu, T.; Luo, L.; Zhong, Z.; Chen, J.; Xiao, H.; Hou, C.; Lou, H.; Chen, Y.; Yang, R.; et al. 2023. Mars: An instance-aware, modular and realistic simulator for autonomous driving. In *CAAI International Conference on Artificial Intelligence*, 3–15. Springer.

Yan, Y.; Lin, H.; Zhou, C.; Wang, W.; Sun, H.; Zhan, K.; Lang, X.; Zhou, X.; and Peng, S. 2024. Street gaussians for modeling dynamic urban scenes. *arXiv preprint arXiv:2401.01339*.

Yang, J.; Ivanovic, B.; Litany, O.; Weng, X.; Kim, S. W.; Li, B.; Che, T.; Xu, D.; Fidler, S.; Pavone, M.; et al. 2023. Emernerf: Emergent spatial-temporal scene decomposition via self-supervision. *arXiv preprint arXiv:2311.02077*.

Yu, M.; Lu, T.; Xu, L.; Jiang, L.; Xiangli, Y.; and Dai, B. 2024. Gsdf: 3dgs meets sdf for improved rendering and reconstruction. *arXiv preprint arXiv:2403.16964*.

Zhang, K.; Riegler, G.; Snavely, N.; and Koltun, V. 2020. Nerf++: Analyzing and improving neural radiance fields. *arXiv preprint arXiv:2010.07492*.

Zhou, H.; Shao, J.; Xu, L.; Bai, D.; Qiu, W.; Liu, B.; Wang, Y.; Geiger, A.; and Liao, Y. 2024a. Hugs: Holistic urban 3d scene understanding via gaussian splatting. In *Proceedings of the IEEE/CVF Conference on Computer Vision and Pattern Recognition (CVPR)*, 21336–21345.

Zhou, X.; Lin, Z.; Shan, X.; Wang, Y.; Sun, D.; and Yang, M.-H. 2024b. Drivinggaussian: Composite gaussian splatting for surrounding dynamic autonomous driving scenes. In *Proceedings of the IEEE/CVF Conference on Computer Vision and Pattern Recognition (CVPR)*, 21634–21643.

Supplemental Material for DHGS: Decoupled Hybrid Gaussian Splatting for Driving Scene

In the supplementary material, we introduce more details on the method and implementation in Sec. A. Extra experimental results are illustrated in Sec. B.

A. Implementation Details

Initial PCD with sky sphere. To deal with the floaters phenomenon in new perspectives, we devise a simple yet effective strategy. We construct a hemispherical virtual sky point cloud layer surrounding the LiDAR point clouds. The radius and center of this sky point cloud were calculated based on the scale of the and the average distribution of the LiDAR points, aiming to accurately mimic the spatial properties of the sky. Additionally, we apply appropriate coloring to the sky point cloud to ensure its visual fidelity, which is shown in Figure 7. For fairness, we integrate this sky sphere point cloud mechanism into all comparative methods.



Figure 7: Visualization of incorporating a sky sphere point cloud to the initial point cloud.

Sigmoid distance constraint. In addition to optimizing the road model, we also utilize a distance constraint mechanism for the environmental model. Rather than directly applying distance regularization to the offsets, we adopt a more restrictive approach, overlaying a sigmoid function on the offsets. This achieves effective boundary control over the offsets. Specifically, we implement the transformation using the following formula:

$$\mu_k = x_v + \lambda_\sigma \cdot (2 \cdot \text{sigmoid}(\mathcal{O}_v \cdot l_v) - 1),$$

where x_v refers to the coordinate of the anchor point, μ_k refers to the center coordinates of the k -th neural Gaussian corresponding to the anchor. l_v and \mathcal{O}_v represent scaling factor and offset vector respectively. This design ensures that the offsets are strictly confined within a reasonable and finite range, thereby preventing the generation of neural Gaussian ellipsoids that are excessively distant from their anchor points. Consequently, the power of the environmental model to represent fine details is significantly enhanced.

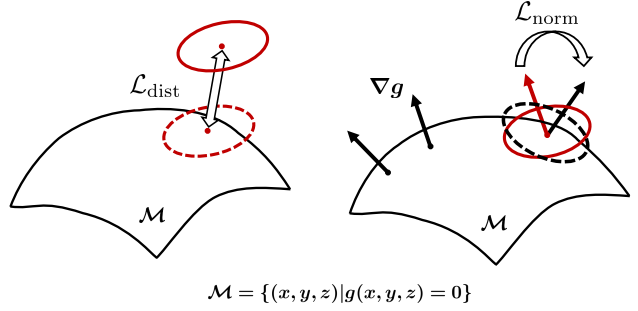


Figure 8: The simplified sketch of distance constraint and normal constraint guided by the zero-level set of SDF, the function g refers to the ideal pretrained SDF.

Regularization loss. The total variation regularization \mathcal{L}_{tv} (Rudin and Osher 1994) is applied in this study to refine the rendered pixel depths. The depth map can be generated through a rendering process similar to the one we calculate color: $D = \lambda_r D_r + \lambda_e D_e$, to maintain the continuity of D near boundaries of two depth maps, the TV regularizer can be represented as:

$$\mathcal{L}_{\text{tv}} = \sum_{\tilde{M}^{i,j} \neq 0} ((D^{i,j-1} - D^{i,j})^2 + (D^{i+1,j} - D^{i,j})^2)^{\frac{1}{2}}.$$

The SDF regularizer \mathcal{L}_{sdf} , inspired by NeuSG originally optimizing the positions and orientations of 3D Gaussians, is applied in this paper similarly to 2D Gaussians. Specifically, we leverage the gradient direction of the pre-trained SDF to guide the orientation updates of the 2D Gaussians, while simultaneously constraining their disk centers to align with the SDF. This approach ensures a seamless integration which is intuitively illustrated in Figure 8.

B. Experimental results

Free-view Novel View Synthesis Settings. We conduct four transformations to the pose of the camera relative to the vehicle, including rotations and translations. The detailed variation amplitudes for the front, front-left, and front-right camera under each transformation are presented in Table 3, where *Translation* denotes the translation distances of the camera along the x , y , and z axes in meter, and *Rotation* represents the rotation angles along the *yaw*, *pitch*, and *roll* axes in degree. Figure 9 depicts the differences in the four transformed camera poses compared to the original Waymo setup.

Qualitative result on Waymo dataset. In addition to the quantitative metrics elaborated in the main document, we attach additional qualitative results to provide a more intuitive performance evaluation of each method. As shown in Figures 10, 11, and 12, the qualitative results indicate that our method achieves the best visualization result in the modeling of both environmental backgrounds and road structures, demonstrating superior performance in scene reconstruction, novel view synthesis and free-view novel view synthesis.

Setting	front-left		front		front-right	
	Translation	Rotation	Translation	Rotation	Translation	Rotation
Set1	(0.5, 0.5, 0)	(0, 0, 0)	(1, 0, 0)	(0, 0, 0)	(0.5, -0.5, 0)	(0, 0, 0)
Set2	(0.5, 0.5, -0.5)	(0, 0, 0)	(1, 0, 0)	(0, 0, 0)	(0.5, -0.5, -0.5)	(0, 0, 0)
Set3	(0.5, 0.5, -0.5)	(10, 0, 0)	(1, 0, 0)	(0, -10, 0)	(0.5, -0.5, -0.5)	(-10, 0, 0)
Set4	(0, 1, 0)	(0, 0, 0)	(0, 1, 0)	(0, 0, 0)	(0, 1, 0)	(0, 0, 0)

Table 3: The table illustrates four different parameter settings for free-view novel view synthesis, where *Translation* refers to translation component, *Rotation* refers to rotation component, the corresponding three numbers are the lengths of translation in meter and the magnitudes of three Euler angles for rotation in degree.

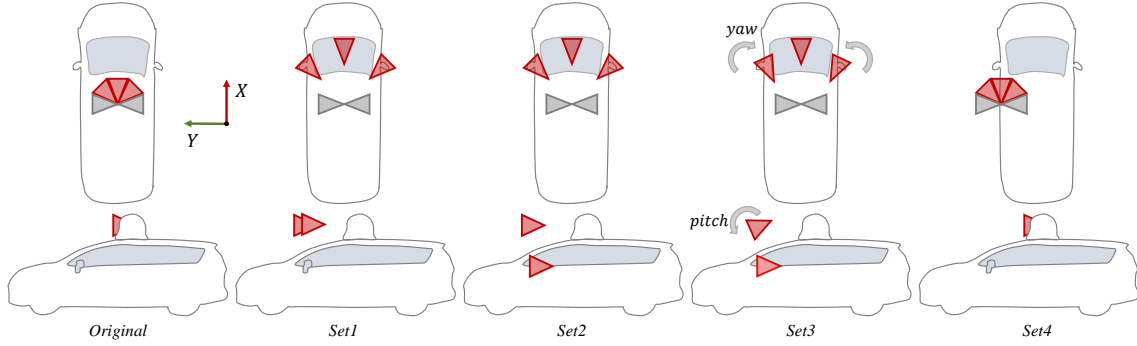


Figure 9: The camera layouts after applying the four settings of camera pose. The top row represents the camera layouts after applying various camera pose settings from a bird's eye view, while the bottom row shows the same transformations from a side view.



Figure 10: Qualitative comparisons on the Waymo dataset, the highlighted regions demonstrate that our method achieves the best rendering quality for both scene reconstruction in the left column and novel view synthesis in the right column.

Free-view Novel View Synthesis

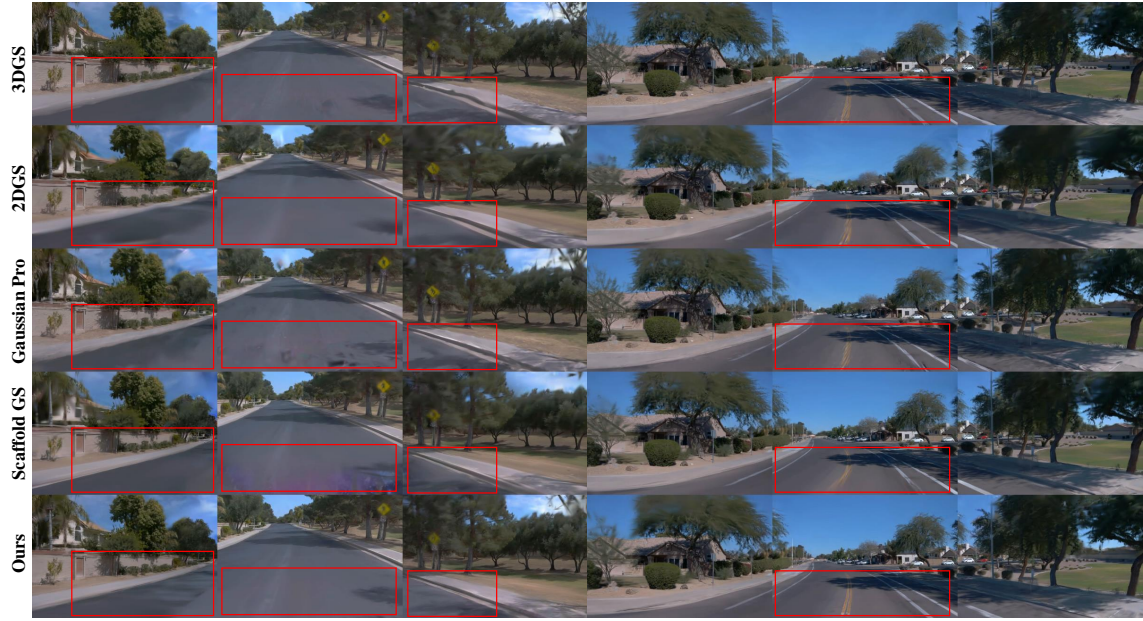


Figure 11: Qualitative results of free-view novel view synthesis under different scenarios, with the left column presenting the outputs from *Set3* and the right column showing those from *Set4*. The highlighted red boxes demonstrate that our method excels in capturing fine details both in terms of geometry and appearance.

Free-view Novel View Synthesis



Figure 12: Qualitative results of free-view novel view synthesis under different scenarios, with the left column presenting the outputs from *Set3* and the right column showing those from *Set4*. The highlighted red boxes demonstrate that our method excels in capturing fine details both in terms of geometry and appearance.